International Journal of Heat and Mass Transfer 78 (2014) 393–407

Contents lists available at ScienceDirect

International Journal of Heat and Mass Transfer

journal homepage: www.elsevier.com/locate/ijhmt

A unified model for Digitized Heat Transfer in a microchannel

Peter Zhang [a,1], Kamran Mohseni [a,b,*]

[a] Department of Mechanical and Aerospace Engineering, University of Florida, 1064 Center Dr. Rm 150, Gainesville, FL 32611, United States
[b] Department of Electrical and Computer Engineering, University of Florida, 1064 Center Dr. Rm 150, Gainesville, FL 32611, United States

ARTICLE INFO

Article history:
Received 5 February 2014
Received in revised form 6 June 2014
Accepted 8 June 2014

Keywords:
Digitized Heat Transfer
Microchannel

ABSTRACT

Digitized Heat Transfer (DHT) is a novel method of adaptive thermal management for high powered devices that uses discrete microdroplets to remove heat. In this paper, the heat transfer characteristics of DHT are investigated for parallel plate and axisymmetric circular microchannels using scale analysis and numerical simulations. DHT in axisymmetric microchannels are also studied using experimental tests. Through scale analysis, it is found that DHT is quantified by the Nusselt number (Nu) and is a function of the Reynolds number (Re), Prandtl number (Pr), nondimensional axial distance (x/D_H), and droplet aspect ratio ($\mathcal{AR}$). In simulation and experiment, Nu shows a direct relationship with Re and Pr as well as an inverse relationship with $\mathcal{AR}$. Using the Graetz problem as a model, new scaling relations are proposed for the axial distance, x, and Nu in an effort to collapse the Nu curves that exist for different flow parameters. To align the characteristic oscillations of Nu found in DHT, x is scaled by the droplet circulation length, L_{circ}, to create a new nondimensional axial distance, $x_{circ} = \frac{x}{L_{circ}}$. In order to match the overall magnitude, Nu scaling is derived based on the two different modes of heat transfer that occur before and after one circulation length. Prior to one circulation length, heat transfer is characterized by thermal boundary layer growth and the scaling parameter is determined to be $f_1 = \sqrt{\frac{RePr}{\mathcal{AR}}}$. After one circulation length, recirculation of heat is dominant and a scaling parameter f_2 is found to be a linear function of $1/\mathcal{AR}$. f_2 is modeled by the equation $f_2 = \frac{c_1}{\mathcal{AR}} + c_2$ where c_1 and c_2 are dependent on Re and Pr. The two scaling constants are merged using an inverse tangent weighting function (w) so that a fully scaled Nusselt number, Nu^*, is defined by $Nu[(1/f_1)(1-w) - (1/f_2)w]$. Using this unified model, numerical and experimental data are reduced to a single curve that depicts the heat transfer to any digitized flow. In the future, this model will be helpful in comparing various DHT systems as well as enabling the design of powerful and efficient DHT based thermal management systems.

1. Introduction

One of the largest challenges facing current and future electronic devices is adequate thermal management. Improper cooling of devices results in high temperatures that can reduce performance, decrease life spans, or even cause catastrophic failure. This problem has only been exacerbated as devices have become smaller and more powerful. Already, high performance devices are producing heat fluxes on the order of 10^3 W/cm^2 [1,2] and are expected to increase to rates greater than 2500 W/cm^2 [3]. In comparison, traditional forms of cooling such as air based forced convection is only capable of heat removal on the order of 10^{-1} W/cm^2. Clearly, traditional forms are insufficient for state-of-the-art systems, however they are also rapidly becoming insufficient for basic personal computer demands as well. To address the growing demands, engineers have turned to liquid based cooling with various implementation schemes that are capable of significantly higher heat transfer rates.

Some of the liquid cooling schemes that have been previously studied include microjet devices [4], thermionic cooling [5,6], thermoelectric microcoolers [7], and microchannel cooling [8]. Each of these methods have unique advantages and disadvantages, but they all seek a balance between performance, cost, and reliability. While some of these methods have achieved extremely high heat transfer rates, they sacrifice cost and reliability. For example, Silverman et al. reported 2000 W/cm^2 in microjet devices using liquid metals [9] and Hirshfeld et al. reported 1500 W/cm^2 in

* Corresponding author at: Department of Mechanical and Aerospace Engineering, University of Florida, 1064 Center Dr. Rm 150, Gainesville, FL 32611, United States. Tel.: +1 (352) 273 1824.
E-mail addresses: peter.zhang@ufl.edu (P. Zhang), mohseni@ufl.edu (K. Mohseni).
URL: http://enstrophy.mae.ufl.edu/ (K. Mohseni).
[1] Tel.: +1 (303) 895 5698.

http://dx.doi.org/10.1016/j.ijheatmasstransfer.2014.06.018
0017-9310/

Nomenclature

A	liquid A
a	sharpness of weighting function
$\mathcal{AR}$	droplet aspect ratio
B	liquid B
b	location of transition in weighting function
c_p	specific heat
c_1	coefficient of f_2 scaling function
c_2	coefficient of f_2 scaling function
D	diameter of axisymmetric channel
D_H	hydraulic diameter
DHT	Digitized Heat Transfer
$EWOD$	Electrowetting On a Dielectric
$\mathbf{f}$	body force
f_1	Nu scaling constant for $x_{circ} < 1$
f_2	Nu scaling constant for $x_{circ} > 1$
h	heat transfer coefficient
H	height of parallel plate channel
k	thermal conductivity
L	length along x-axis
L_A	length of a droplet of fluid A
L_B	length of a droplet of fluid B
L_D	length of a droplet
N_Γ	ratio of diffusion time scale to convection time scale
Nu	Nusselt number
Nu^*	scaled Nusselt number
Nu_{avg}	time averaged Nu
Nu_{Graetz}	Nu curve for the Graetz problem
n	liquid fraction
p	pressure
Pe	Peclet number
Pr	Prandtl number
q''	heat flux
r	axis in radial direction
Re	Reynolds number with D_H as the characteristic length
Re_L	Reynolds number with L as the characteristic length
t	time
T	temperature
T_w	temperature at inner wall of channel
T_b	droplet bulk temperature
T_0	inlet temperature
u	velocity component parallel to the x-axis
U	bulk velocity along the x-axis
$\mathbf{v}$	velocity vector
w	scaling weight function
x	axis parallel to the line of symmetry in a fixed reference frame
x'	axis parallel to the line of symmetry in a moving reference frame
x_{circ}	axial distance nondimensionalized by circulation length
x^*	Graetz number
X_T	length along x which a flow becomes thermally fully developed
y	axis normal to the wall in a parallel plate channel
α	thermal diffusivity
δ_s	dirac delta function
δ_T	thermal boundary layer thickness
κ	curvature of the interface
λ	length of droplet fluid A and B combined
μ	dynamic viscosity
ρ	density
σ	surface tension
τ_{diff}	diffusion time scale
τ_{circ}	recirculation time scale
θ	nondimensional temperature
θ_w	nondimensional wall temperature
θ_{avg}	average nondimensional temperature

microchannels [10]. While effective for high heat flux cooling, these methods are limited by high pumping pressure, susceptibility to mechanical failure, and lack of adaptability. A relatively new method of cooling that is the focus of this paper is Digitized Heat Transfer (DHT) [11–13], a method that has the potential to provide a reliable, highly adaptable, and efficient thermal management solution.

DHT is a method of thermal management that utilizes discrete microdroplets translating across heated surfaces to remove excess heat. Several methods of droplet transport have been proposed including dielectrophoresis [14], acoustic waves [15] thermocapillarity [16], and electrowetting [17,18]. Among these methods, Electrowetting On a Dielectric (EWOD) has become the most popular due to its low energy consumption, high actuation velocities, and programmability. EWOD uses electrodes beneath a dielectric layer to manipulate droplet wetting behavior. On an array of electrodes, voltage can be applied such that the electrode beneath the leading edge of the droplet is always activated. This in turn will cause droplet motion in the direction of the activated electrode. One of the primary advantages of this method is its mechanical simplicity. The system does not require any pumps or valves, thus creating a system that is less prone to failure. Furthermore, droplet paths are fully programmable and can be reconfigured by simply editing a computer program. This allows for real time droplet path optimization for changing temperature distributions. Fig. 1 shows a conceptual representation of a simple DHT device that could transport discrete droplets using any of the methods mentioned previously. As seen in the theoretical device, droplets can be transported across the heated surface along hundreds of different paths, creating a flexible and adaptable system. While electrodes are patterned directly onto the heated surface in Fig. 1, an alternative configuration could pattern electrodes on a separate plate that is placed opposing the heated surface. Coolant would flow between the heated surface and the actuation plate, thus creating a more modular system. In terms of heat transfer, digitized flows have shown higher heat transfer rates than continuous flows with equivalent mass flow rates [12,13]. While heat transfer to digitized flow has been studied previously [12,13,19–25], most of these studies have been limited to specific Reynolds numbers, Prandtl numbers, and aspect ratios. Amongst these studies, multiple parameters were simultaneously

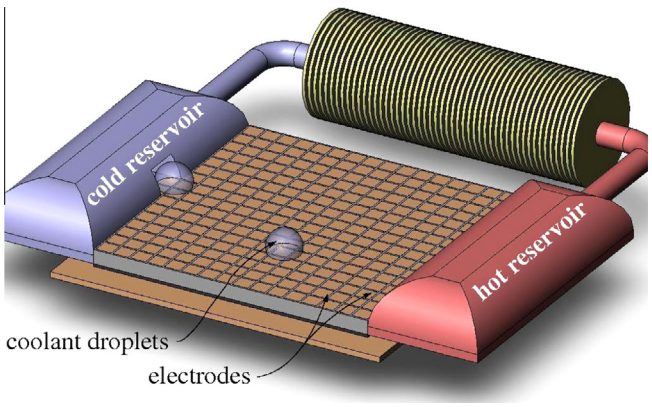

Fig. 1. DHT concept device.

changed, thus making it difficult to isolate the effect of individual parameters. Therefore, a unified model that provides a means of comparing various results is needed.

This paper builds off the studies [26,27] using numerical and experimental methods to identify proper scaling of the governing nondimensional parameters and to create a unified model. First, the problem being studied is established along with the numerical and experimental methods that are used. Next, the governing nondimensional parameters are identified. Afterwards, the numerical results are discussed and are used to propose a new scaling of the nondimensional parameters. Last, analysis of experimental results is performed to verify the numerical findings and scaling. While this paper is focused on heat transfer, the transport of mass behaves similarly suggesting that the results and models could potentially be applied to other applications such as multiphase monolith reactors [28] or droplet microfluidics [29].

2. Problem geometry

The problem being considered in this paper is heat transfer in a digitized flow consisting of two immiscible fluids within a microchannel. The channel is either a parallel plate or axisymmetric channel and the fluids can be either gaseous or liquid as long as they remain immiscible. Even though a microchannel is simpler than an EWOD configuration, it maintains many of the same heat transfer characteristics [21,13]. Fig. 2 shows a schematic of the configuration. H and D are the height and diameter of a parallel plate channel and axisymmetric channel. x is the axis parallel to the axis of symmetry whose origin resides at the start of the heated wall. y and r are the wall normal axes. L_A and L_B are the lengths of the droplets consisting of fluid A and B while λ is the combined length of the droplets. In a reference frame moving with the droplet, the axis parallel to the axis of symmetry is defined as x' whose origin is located at the trailing interface as seen in Fig. 3. For the simulations, L_D is the wall contact length of the droplet and is used as a substitute for either L_A or L_B. L is the distance between the stationary reference frame and the moving reference frame. The problem assumes that the flow is hydrodynamically fully developed, symmetric about the centerline, isothermal at the entrance, and subject to either constant temperature or constant heat flux at the wall. This configuration is similar to the classical Graetz problem which characterizes heat transfer in a continuous flow within a channel under the same assumptions listed previously. Since the Graetz problem has been well studied and is fairly similar, it will be used as a benchmark and model for developing a fundamental understanding of DHT.

Thus far, four similar but distinct problems have been identified. They include the four unique combinations of either a parallel

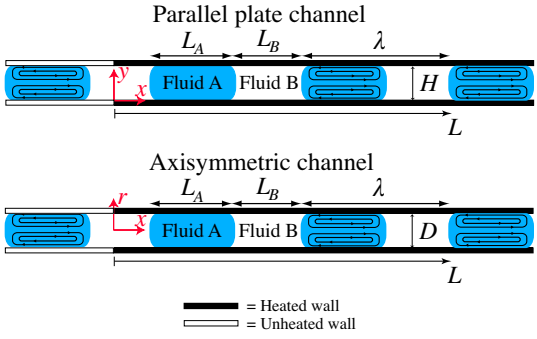

Fig. 2. Problem geometry in a fixed reference frame. L_A is the length of the droplet consisting of fluid A and L_B is the length of the fluid B droplet. λ is the combined length of droplets A and B. H and D are the height and diameter of the channel. x is the axis parallel to the axis of symmetry whose origin starts at the start of the heated wall. y and r are the wall normal axes. L is the distance a droplet has traveled from the start of the heated wall.

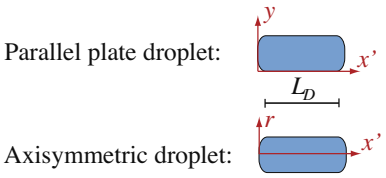

Fig. 3. Reference frame within a moving droplet for both parallel plate and axisymmetric geometries.

plate channel or axisymmetric channel subject to constant wall temperature or constant wall heat flux. In the following sections, discussion of the numerical results will be limited to a parallel plate subject to either a constant wall temperature or constant wall heat flux. A summary of the key results for the axisymmetric case will be presented, however a detailed discussion will not be conducted since the majority of the fundamental principles that govern the phenomenon remain the same.

3. Numerical method

In order to numerically simulate heat transfer to a digitized flow, a single phase moving reference frame technique was used. This method had a low computational cost that made a large number of simulations feasible. The numerical simulations in this paper solved the equations governing the balance of mass and heat transfer given by

$$\nabla \cdot \mathbf{v} = 0, \tag{1}$$

$$\rho\left(\frac{\partial \mathbf{v}}{\partial t} + \mathbf{v} \cdot \nabla \mathbf{v}\right) = -\nabla p + \mu \nabla^2 \mathbf{v} + \mathbf{f} + \sigma \kappa \delta_s \mathbf{n}, \tag{2}$$

$$\frac{\partial T}{\partial t} + \mathbf{v} \cdot \nabla T = \alpha \nabla^2 T, \tag{3}$$

where $\mathbf{v}$ is the velocity vector, ρ is the density, t is time, p is pressure, μ is viscosity, $\mathbf{f}$ is the body force, σ is the surface tension coefficient, κ is the curvature, δ is the dirac function isolating effects to the interface, $\mathbf{n}$ is interface normal vector, T is the temperature, and α is the thermal diffusivity. Simulations were made using the Marker and Cell Method [30] on a staggered grid in 2D cartesian and axisymmetric coordinates. To solve for the velocity field, time was approximated using a forward Euler scheme and spatial terms used a second order accurate centered finite difference. Nonlinear terms were treated explicitly and for fast flows, an upwinding approach was applied to the convective terms. The viscous terms were treated implicitly and a pressure correction step was taken to ensure continuity of the flow. Boundary conditions at the walls were set to no slip, zero normal velocity, and constant temperature or constant heat flux. At the interfaces, boundary conditions were set to a free-slip impermeable boundary with zero heat flux. Temperature simulations were conducted using nondimensional temperature (θ) defined as

$$\text{Constant wall temperature}: \quad \theta(x,x') = \frac{T_w - T(x,x')}{T_w - T_0},$$

$$\text{Constant wall heat flux}: \quad \theta(x,x') = \frac{T(x,x') - T_0}{q'' \frac{D_H}{k}},$$

where T_w is the wall temperature, T_0 is the inlet temperature, q'' is the heat flux, D_H is the hydraulic diameter, and k is the thermal conductivity. Heat transfer was quantified using Nusselt number which is defined as $Nu = \frac{hD_H}{k}$ where h is the heat transfer coefficient. For the results presented below, the droplet averaged Nu is expressed as

$$\text{Constant wall temperature}: \quad Nu(x) = \frac{1}{L_D}\int_0^{L_D} \frac{\left.\frac{\partial\theta(x,x')}{\partial y}\right|_{\text{wall}} D_H}{\theta_{\text{avg}}(x,x')}dx',$$

$$\text{Constant wall heat flux}: \quad Nu(x) = \frac{1}{L_D}\int_0^{L_D} \frac{D_H}{\theta_w(x,x') - \theta_{\text{avg}}(x,x')}dx',$$

using nondimensional temperature. θ_{avg} is defined as

$$\text{Parallel plate channel}: \quad \theta_{\text{avg}}(x,x') = \int_0^H \theta(x,x',y)\frac{u(x',r)}{U}dy,$$

$$\text{Axisymmetric channel}: \quad \theta_{\text{avg}}(x,x') = \frac{\int_0^{D/2} u(x',r)\theta(x,x',r)rdr}{\int_0^{D/2} u(x',r)rdr}.$$

4. Experimental set up

The experimental tests were conducted using a test channel composed of a T-junction and heated test section pictured in Fig. 4. Using a WPI SP250I and Chemyx 10020 Fusion 200 syringe pump, water and air were pumped into separate arms of the T-junction at constant flow rates as depicted in Fig. 5. By supplying different water and air flow rates, a wide variety of digitized flows were generated in the third arm of the junction, which were then captured by a high speed camera to determine velocity and aspect ratio. Using this simple method, consistent digitized flows are generated with varying Reynolds numbers, aspect ratios, and volume fractions.

After the digitized flow is formed, it passes into a stainless steel microchannel with a 1.5 mm inner diameter and 2 mm outer diameter. The flow is allowed to become hydrodynamically fully developed and is then subject to constant heat flux at the wall. Heating of the wall is achieved by using two thin brass contacts to joule heat the channel. Using a FLIR A655sc infrared (IR) camera, temperature measurements were taken to determine the surface temperature of the channel. To improve the precision and accuracy of the measurements, the channel was coated with a thin layer of matte black paint to reduce reflections and increase emissivity. The IR camera is equipped with a 640×480 pixel sensor which was used in conjunction with a 24.8 mm focal length lens. This gives a minimum spot size of 0.17 mm/pixel. Thus, across the 2 mm channel there were approximately 11 measurement points. Furthermore, images of the heated channel were taken at 50 frames per second giving this experimental configuration high temporal and spatial resolutions.

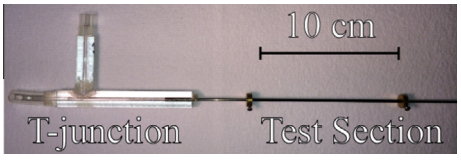

Fig. 4. Experimental test channel including droplet generating T-junction and heated stainless steel test section.

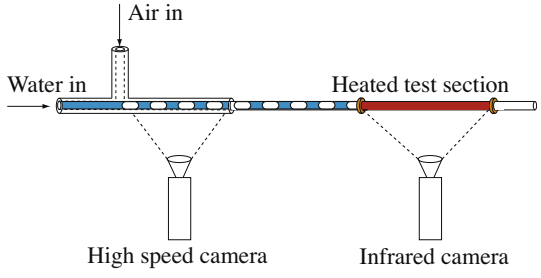

Fig. 5. Schematic of experimental test set up. High speed camera is used to determine velocity and aspect ratio of digitized flow. Infrared camera is used to measure surface temperature of the test section.

4.1. Experimental set up validation

To ensure that accurate temperatures were measured, the experimental set up was calibrated by first measuring the heat transfer in a continuous flow and comparing it to well documented theoretical values [31,32]. Theoretical *Nu* values were predicted using the equations below taken from [32] where x^* is the Graetz number and is defined as $x/(DRePr)$.

$$Nu = \begin{cases} 1.302(x^*)^{-\frac{1}{3}} - 1, & x^* \leqslant 0.00005, \\ 1.302(x^*)^{-\frac{1}{3}} - 0.5, & 0.00005 \leqslant x^* \leqslant 0.0015, \\ 4.364 + 8.68(10^3 x^*)^{-0.506} e^{-41x^*}, & x^* \geqslant 0.0015. \end{cases}$$

By adjusting IR camera parameters such as emissivity, reflected temperature, and ambient temperature, temperature measurements were calibrated to match known temperature profiles. Fig. 6 shows the independently measured Nusselt curve of the calibrated IR camera for the Graetz problem. During both thermal development and steady state, the experimental *Nu* values agree well with theory and indicate that the camera accurately measures surface temperature.

5. Governing nondimensional parameters

The heat transfer phenomenon being studied is governed by the dimensional parameters h, H, k, x, ρ, μ, U, c_p and L_D. These represent the heat transfer coefficient, channel height, thermal conductivity, axial distance, density, viscosity, mean velocity, specific heat, and length of the droplet respectively. Heat transfer is quantified by h and is a function of eight other parameters. In this form, observations can only be made for specific flows and it is difficult to make general statements about heat transfer to digitized flow as a whole. However, using Buckingham Pi theorem [33], the nine dimensional parameters can be reduced into five nondimensional parameters: *Nu*, *Re*, *Pr*, x/H, and aspect ratio ($\mathcal{R} = L_D/H$). Using these, flows can be lumped together into groups with similar nondimensional parameters and more general statements can be made for DHT. For the parallel plate configuration, the effects of *Re*, *Pr*, x/H and $\mathcal{R}$ on *Nu* are investigated. In the case of an axisymmetric

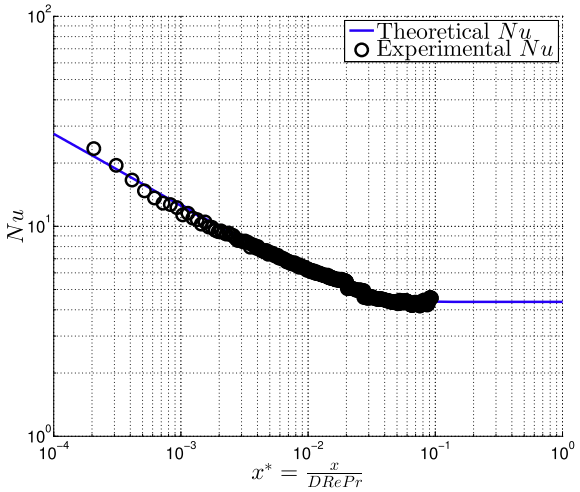

Fig. 6. *Nu* for a continuous flow subject to constant wall heat flux in an axisymmetric microchannel (Graetz Problem).

channel, diameter (D) is used in place of H and Nu is investigated with respect to Re, Pr, x/D and $\mathcal{R}$.

6. Droplet hydrodynamics

In order to fully understand heat transfer to a digitized flow, it is important to fully characterize and understand the hydrodynamics as it has a significant effect on heat transfer. In 2008, Baird and Mohseni conducted a numerical study of a translating droplet using a single phase, moving reference frame technique [13]. They found that a translating droplet contained a flow field that consisted of two counter rotating vortices. This is observed in Fig. 7 where the droplet flow and temperature field have been reproduced using the numerical method described above. In the recirculating regions, the induced wall normal velocity enhances heat transfer as compared with the Graetz problem.

Fig. 8 shows the axial velocity profiles, u, at various cross sections within a droplet from a fixed reference frame. In agreement with [13], the velocity profile at the center of the droplet ($0.5L_D$) is parabolic and closely resembles the Poiseuille profile. Near the leading interface ($0.95L_D$), the velocity profile is non-parabolic and has a shape that approaches a slug profile. At the trailing interface ($0.05L_D$), the magnitude of the peak velocity is less than the Poiseuille profile but retains its parabolic shape, indicating that the velocity profiles within the droplet are not symmetric about $x' = 0.5L_D$. A study of the effects of $\mathcal{R}$ and Re on droplet hydrodynamics was conducted where it was found that:

- Increases in Re cause increases in nondimensional velocity magnitude at the axis of symmetry and near the wall (Fig. A.31(b)),
- A combination of low $\mathcal{R}$ and high Re causes inflection points in velocity profiles, which indicate potential susceptibility to turbulence.
- Droplets with aspect ratios less than one begin to converge to a different class of flow where the two vortices seen in Fig. 7 do not penetrate to the axis of symmetry and are instead separated by a region of fluid with no wall normal velocity (Fig. A.32).

Detailed data supporting these observations can be found in Appendix A.

7. Heat transfer results

7.1. Effects of $\mathcal{R}$, Pr and Re on Nu for DHT

In 2008, Baird and Mohseni [13] conducted a study on heat transfer in a digitized flow and its dependency on axial distance

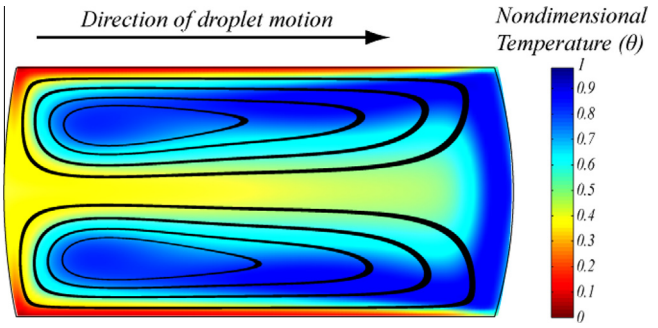

Fig. 7. Droplet streamlines and nondimensional temperature field within a parallel plate channel subject to constant wall temperature. Image taken from a moving reference frame at $x/H = 3.75$ for $Re = 100$, $\mathcal{R} = 2$, and $Pr = 6$ with a contact angle of 105°.

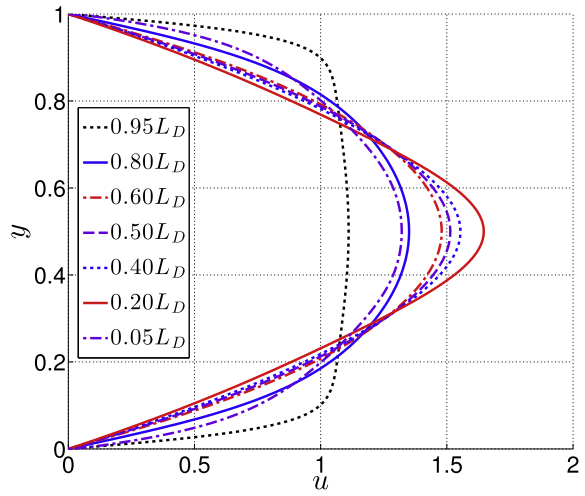

Fig. 8. Droplet u velocity along various cross sections for a droplet in a parallel plate channel. $Re = 100$, $\mathcal{R} = 2$.

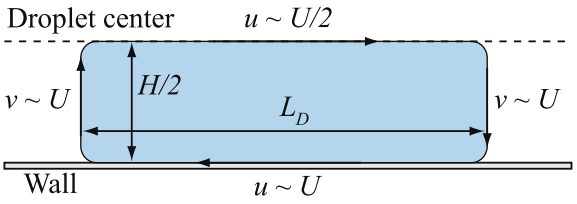

Fig. 9. Velocity scales of droplet interfaces for $0 \leqslant y \leqslant H/2$ in a parallel plate channel from a moving reference frame.

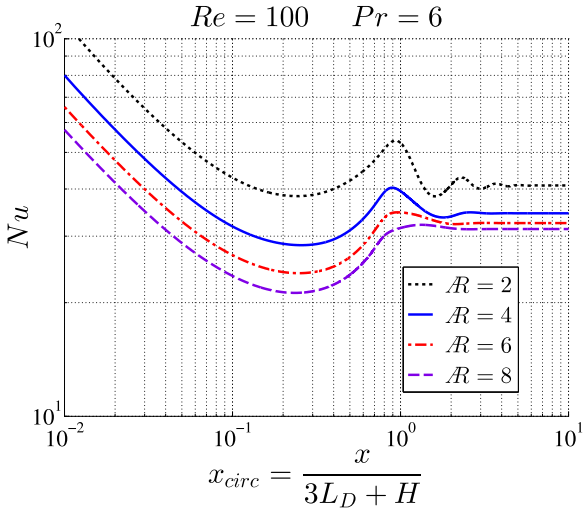

Fig. 10. Nu for a digitized flow in a parallel plate channel with constant wall temperature and varying aspect ratio ($\mathcal{R} = L_D/H$).

and aspect ratio. They found that as heat diffuses into a droplet, the two internal vortices convect hot fluid away from the wall and towards the center of the droplet as seen in Fig. 7. Eventually, this hot fluid is circulated back to the front of the droplet and is in contact with the wall while heat diffuses towards the center of the vortices. Using Nu to characterize the heat transfer rate, they observed that Nu initially showed a steady decrease in magnitude followed by periodic oscillations until finally reaching steady state as seen in Fig. 10. Additionally, they observed that as $\mathcal{R}$ decreased, the magnitude of Nu increased and exhibited a higher number of

oscillations before reaching thermal steady state. Originally, in [13], the circulation time scale (τ_{circ}) and circulation length (L_{circ}) was approximated by $(2L_D + H)/U$ and $2L_D + H$ respectively for a parallel plate channel. Using $L_{circ} = 2L_D + H$ to scale x, they were able to approximately align the peaks in Nu along the x-axis, however the peaks did not occur at integer values. A more accurate prediction is achieved by using a better estimate for horizontal velocity at the droplet centerline, namely $u \sim U/2$. The approximate droplet velocities are shown in Fig. 9, and a more accurate circulation time and length are defined as

$$\text{Parallel plate channel}: \quad \tau_{circ} = (3L_D + H)/U, \tag{4}$$

$$L_{circ} = 3L_D + H. \tag{5}$$

Scaling axial distance, x, by $L_{circ} = 3L_D + H$ yields the nondimensional axial distance, x_{circ}, and aligns the oscillations in Nu at integer values as seen in Fig. 10.[2]

Before conducting additional numerical simulations, the ratio of the diffusion time scale, $\tau_{diff} = H^2/\alpha$, and the circulation time scale, τ_{circ}, can be used to predict the effects of $\mathcal{R}$, Re, and Pr on Nu. This diffusion-recirculation ratio is defined as

$$N_\Gamma = \frac{\tau_{diff}}{\tau_{circ}} = \frac{H^2/\alpha}{(3L_D + H)/U} = \frac{RePr}{3\mathcal{R} + 1} \tag{6}$$

and was first reported in [13]. The magnitude of N_Γ approximates the relative contribution of diffusion in comparison to convection and is positively correlated to Nu, the nondimensional parameter that is physically interpreted as the ratio of convection over diffusion. If N_Γ is less than one, τ_{diff} is smaller than τ_{circ} and predicts low Nu magnitudes where diffusion of heat within the droplet acts faster than recirculation. Based on Eq. (6), N_Γ less than unity is characteristic of flows with large $\mathcal{R}$ and small Re or Pr. For N_Γ greater than one, the opposite is true. τ_{circ} is smaller than τ_{diff} suggesting larger Nu magnitudes for flows with small $\mathcal{R}$ and large Re or Pr. The negative correlation between $\mathcal{R}$ and Nu agrees with the numerical findings of Baird and Mohseni [13] as well as the experimental findings of Walsh et al. [19]. In the following sections, numerical and experimental analysis confirms the positive correlation between Nu, Re and Pr.

Fig. 10 depicts numerically computed Nu versus $x_{circ} = \frac{x}{3L_D+H}$. As expected, results show that decreases in $\mathcal{R}$ are correlated with increases in Nu and agrees with the N_Γ analysis above. Fig. 11 shows the effect of Pr on Nu for constant Re and $\mathcal{R}$. As Pr decreases, the magnitude of Nu decreases at all axial distances and fewer oscillations are present before reaching thermal steady state. Fig. 12 demonstrates that smaller Re values are correlated with lower Nu magnitudes and fewer oscillations. Interestingly, it was found that Nu oscillations were only present for $N_\Gamma > 7$, indicating that the τ_{circ} must be seven times smaller than the τ_{diff} in order for recirculation to have a noticeable effect. It should be noted that flows with the same Peclet number ($Pe = RePr$) are not equal, but are slightly different for different Re values. This difference is caused by the slightly different flow fields that exist within a droplet for different Re values. Tests run with varying Re but constant Pe showed slightly sharper oscillations for larger Re values.

Fig. 13 shows Nu variation with respect to $\mathcal{R}$ when subject to a wall with constant heat flux. Similar to the constant wall temperature case, the Nu curves show a steady decrease as x_{circ} increases towards one circulation length. As the curve nears one circulation length, recirculation effects become relevant and periodic oscillations in Nu are observed. In comparison to the constant wall temperature case, the peaks for a constant wall heat flux boundary condition are sharper. This is caused by the different definitions of θ and Nu chosen for each boundary condition. Nu behavior with respect to Re, Pr, and $\mathcal{R}$ remain the same as the constant wall temperature case. In general, the effects of Re, Pr and $\mathcal{R}$ on Nu can be summarized as

- Increase in $Re \rightarrow$ Increase in Nu magnitude and slower decay of Nu peaks.
- Increase in $Pr \rightarrow$ Increase in Nu magnitude and slower decay of Nu peaks.
- Increase in $\mathcal{R} \rightarrow$ Decrease in Nu magnitude and faster decay of Nu peaks.

Next, it is instructive to look at a comparison between DHT in a microchannel and the Graetz problem. One of the first differences that is immediately apparent is the difference in the scaling of the x-axis where the Graetz problem uses the Graetz number

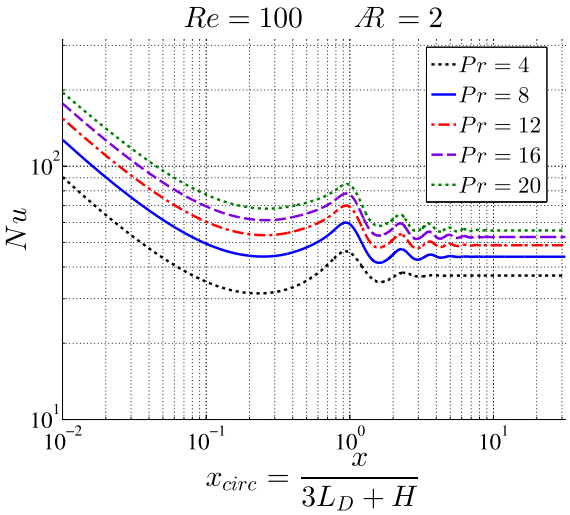

Fig. 11. Nu with respect to x_{circ} for a digitized flow in a parallel plate channel with constant wall temperature.

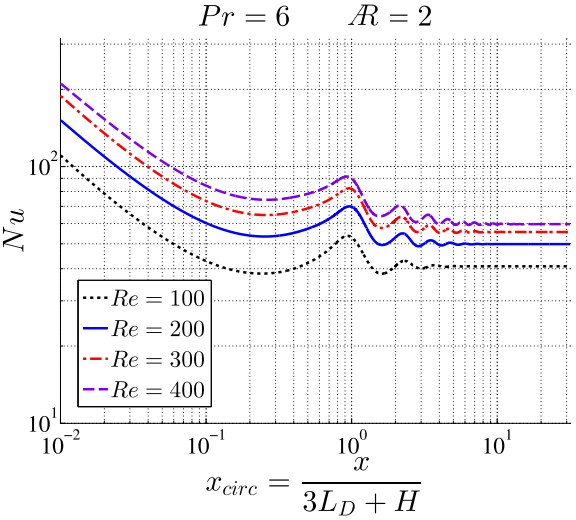

Fig. 12. Nu with respect to x_{circ} for a digitized flow in a parallel plate channel with constant wall temperature.

[2] While the circulation length and time defined in Eqs. (4) and (5) are used for parallel plate geometries, the original definitions found in [13] are retained for axisymmetric channels for simplicity. Axisymmetric circulation time and length are given by $\tau_{circ} = \frac{2L_D+D}{U}$ and $L_{circ} = 2L_D + D$. Note that for an axisymmetric droplet, L_{circ} is slightly shorter than the true circulation length. As a result, the peaks in the Nu curve do not occur at integer values of x_{circ} and are shifted to the right slightly as shown in Fig. 21.

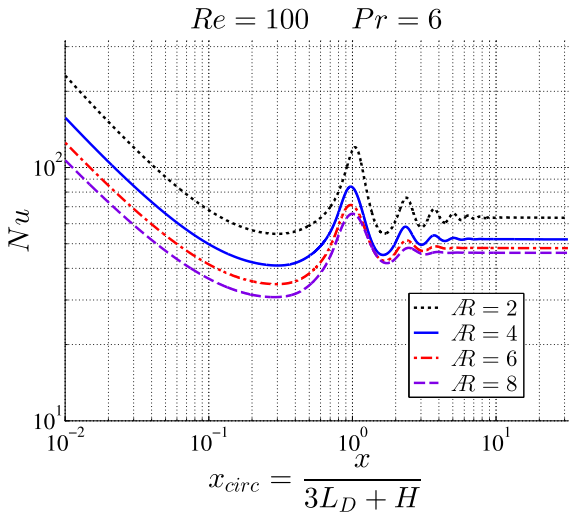

Fig. 13. *Nu* with respect to x_{circ} for a digitized flow in a parallel plate channel with constant wall heat flux.

$\left(x^* = \frac{x}{D_H Re Pr}\right)$ and DHT uses $x_{\text{circ}} = \frac{x}{3L_D+H}$, as seen in Fig. 6 and 10–13. In the following section, the derivation of the Graetz number is reviewed and it will be shown that the Graetz number scaling may not be the most appropriate scaling of x for DHT despite its use in past publications [13,19,25].

7.2. Review of scaling of the spatial coordinate, x, in the Graetz Problem

The Graetz problem considers heat transfer in a fully developed continuous flow in a channel. As mentioned previously, the flow is symmetric about the centerline, has an isothermal entering fluid, and has either uniform wall temperature or constant wall heat flux. The heat transfer is governed by the dimensional variables h, D_H, k, x, ρ, μ, U, and c_p which can be reduced to Nu, Re, Pr, and x/D_H using Buckingham Pi theorem analysis. Therefore, Nu will be a function of Re, Pr, and x/D_H. If Nu is plotted vs x/D_H, it becomes apparent that all the curves are similar for various Re and Pr. The primary difference among the various Nu curves is the axial distance where the flow becomes thermally fully developed, X_T. Therefore, if x is scaled by X_T, Nu will collapse to a single line for all Re and Pr.

To estimate X_T in terms of known flow parameters, scale analysis and boundary layer theory are applied to the governing equations. First, let δ_T be the wall normal length scale in which T changes from T_W to the undisturbed inlet temperature, T_0. The scales for changes in u, x, and y within the thermal development region are identified as

$$u \sim U, \quad x \sim L, \quad y \sim \delta_T.$$

Substituting these length scales into Eq. (3) and simplifying yields

$$\delta_T \sim \frac{L}{Re_L^{1/2} Pr^{1/2}}, \tag{7}$$

where subscript L indicates using L as the length scale for Reynolds number. When the flow is thermally fully developed, δ_T can be approximated by D_H and L by X_T. Using these approximations, Eq. (7) simplifies to

$$\left(\frac{X_T}{D_H Re Pr}\right)^{1/2} \sim 1. \tag{8}$$

From Eq. (8) it becomes clear that $x^* = x/X_T = x/(D_H Re Pr)$, or the well known Graetz number. Additional details of the derivation can be found in [31] and a detailed discussion of heat transfer in laminar flow in ducts can be found in [32].

7.3. Scaling of the spatial coordinate x for DHT

It is now clear that a digitized flow violates the assumptions used to predict the growth of a thermal boundary layer. Violations include different velocity profiles along the droplet's length, existence of wall normal velocity near the interfaces, and non-constant temperature at the upper edge of the thermal boundary layer. Therefore, the approximation of X_T given in Eq. (8) is not appropriate for DHT. This is reinforced by the fact that plots of Nu with respect to $x^* = \frac{x}{D_H Re Pr}$ seen in [13,19,25] show digitized flows reaching thermal steady state at different x-axis values.

In order to obtain a level of understanding similar to the Graetz problem, it is imperative that a new scaling of the spatial coordinate be derived. Motivated by the analysis performed for the Graetz problem, a similar analysis is now applied to DHT. In Figs. 10–13, it can be seen that the primary characteristic lengths of the problem are the L_{circ} and X_T. If axial distance, x, were to be nondimensionalized by X_T, Nu curves would condense so that they would all become fully developed at roughly the same x-axis position, however the oscillations would be misaligned. If axial distance is nondimensionalized by circulation length, a well organized plot is obtained where all the Nu oscillations are aligned as seen in [13] and Figs. 10–13. Therefore, for DHT it is more logical to scale the axial distance (x) by the circulation length (L_{circ}). This choice is also convenient since X_T is not easily approximated using the flow parameters while circulation length is simply $3L_D + H$ (or $2L_D + D$ for the axisymmetric case). This analysis confirms the use of x_{circ} which was previously derived. In terms of governing nondimensional parameters, x_{circ} can be rewritten as $\frac{x/H}{3/\mathcal{R}+1}$.

The next logical step is to derive scaling for the y-axis, Nu, using Re and Pr. This analysis is split into two regions that are defined by $x_{\text{circ}} < 1$ and $x_{\text{circ}} \geqslant 1$ based on the two distinct types of heat transfer behavior observed before and after one circulation length. Fig. 7 shows the developing temperature field prior to one full circulation length where a thermal boundary layer is developing at the walls. The upper edge of the thermal boundary layer and the incoming flow at the leading interface is maintained at the inlet temperature, thus the Nu curve should resemble the Nu curve for the Graetz problem. However, they will not be identical due to the varying velocity profiles along the droplet length and the wall normal velocity. For $x_{\text{circ}} \geqslant 1$, recirculation effects become dominant and the thermal evolution no longer behaves like a developing boundary layer but is rather a balance between diffusion and the recirculation of hot fluid. Since there are two different types of behavior, two separate scalings are needed.

7.4. Scaling of heat transfer (Nu) for $x_{\text{circ}} < 1$ for DHT

In Figs. 10–12 it can be seen that prior to one circulation length ($x_{\text{circ}} < 1$), Nu curves follow the same power law while simply shifted vertically along the y-axis for different $\mathcal{R}$ or Pe. Similar to how x was scaled by the reference length L_{circ}, a reference Nu curve is selected to scale all other Nu curves. For DHT, the reference curve chosen is the lower limit of the problem where Peclet number and aspect ratio equal one. In flows where Pe is less than one, heat diffuses faster than it can be convected, resulting in heat transfer that is dominated by diffusion as well as axial conduction. This results in Nu curves that do not exhibit oscillations and are more similar to heat transfer in slug flows [31]. Similarly, the Graetz problem exhibits different Nu curves when axial conduction is non-negligible [32]. For aspect ratios less than one, the droplet flow field converges to a different hydrodynamic steady state as discussed previously. This different class of flow results in a different mode of heat transfer

than what has been defined as DHT. Additional discussion of flows with small aspect ratios can be found in Appendix A. Scaling by the lower limit leads to the scaling parameter f_1 defined as

$$f_1 = \frac{Nu(Pe, \mathcal{R}, x_{\text{circ}})}{Nu(Pe = 1, \mathcal{R} = 1, x_{\text{circ}})}. \tag{9}$$

By conducting a wide range of numerical simulations, it is found that f_1 is approximated by $\sqrt{Pe/\mathcal{R}}$ such that the y-axis can be scaled as $Nu\sqrt{\mathcal{R}/Pe}$. The results of this scaling are shown in Figs. 14 and 15. For values of x_{circ} less than one, the curves collapse fairly well regardless of Pe or $\mathcal{R}$. At x_{circ} values less than 10^{-2}, curves are essentially the same but slowly begin to diverge as x_{circ} approaches one. As predicted, the curves within the first circulation length resemble the Nu curve of the Graetz problem and scaling by f_1 is not effective for x_{circ} greater than one. It should be noted that while the shape appears similar to the Graetz curve, Nu with respect to x/H for DHT has a larger magnitude and slightly steeper slope than for a continuous flow. This difference is physically justified by the wall normal convection in droplets that transports hot fluid away from the wall resulting in faster thermalization of the droplet. On the other hand, a Poiseuille flow has no convection at the wall. Heat must first diffuse through the non-moving layer of fluid at the wall before it can be convected away. This enhanced convection in DHT caused by wall normal convection is similar to the increased magnitude and steeper slope observed for heat transfer to slug flows where wall tangential convection occurs. Note that all the scaling done here and in the rest of this manuscript is tailored for flows that are dominated by convection. Therefore, for small N_Γ, Nu scaling is not as effective.

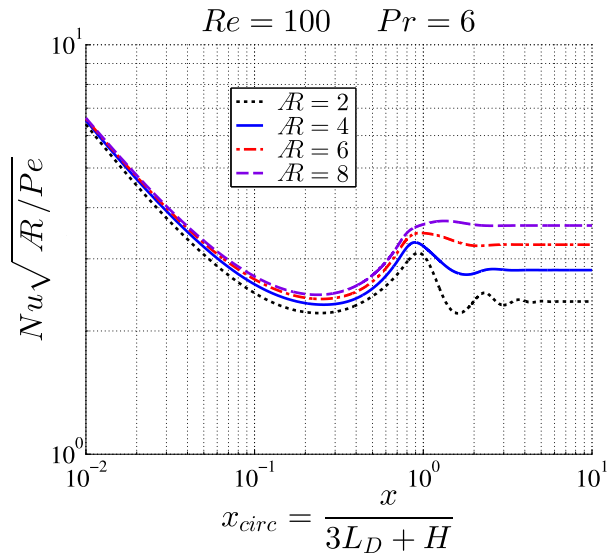

Fig. 14. Scaled Nu with respect to x_{circ} in a parallel plate channel for constant wall temperature.

7.5. Scaling of heat transfer (Nu) for $x_{\text{circ}} \geqslant 1$ for DHT

Next, a scaling for the second heat transfer regime ($x_{\text{circ}} > 1$) is derived. Using the same analysis that was done for $x_{\text{circ}} < 1$, Nu for a thermally fully developed digitized flow is scaled by the thermally fully developed Nu of a continuous flow. The continuous flow is chosen since the previously discussed effect of $\mathcal{R}$ dictates that an $\mathcal{R}$ approaching infinity will have the smallest steady state Nu magnitude. A second scaling constant is defined as

$$f_2 = \frac{Nu(x_{\text{circ}} \to \infty)}{Nu_{\text{Graetz}}(x^* \to \infty)}. \tag{10}$$

For constant Re and Pr values, f_2 varies linearly with respect to $1/\mathcal{R}$ as seen in Fig. 16. Hence, a linear model is defined as $f_2 = c_1/\mathcal{R} + c_2$ to approximately predict the scaling constant. Additional simulations were run for various Pr values, where it was found that c_1 and c_2 are functions of Pr such that the scaling constant can be approximated by

$$f_2 = \frac{c_1}{\mathcal{R}} + c_2, \tag{11}$$

$$c_1 = 2.4Pr^{0.41} - 1.7, \tag{12}$$

Constant wall temperature :

$$c_2 = -2.4Pr^{-0.15} + 5.6 \tag{13}$$

for $Re = 100$. Fig. 16 depicts f_2 where the discrete points denote the results from the numerical simulations and the dashed line denotes the predicted scaling constant given by Eqs. (11)–(13). The majority of the points show excellent agreement with the model, however

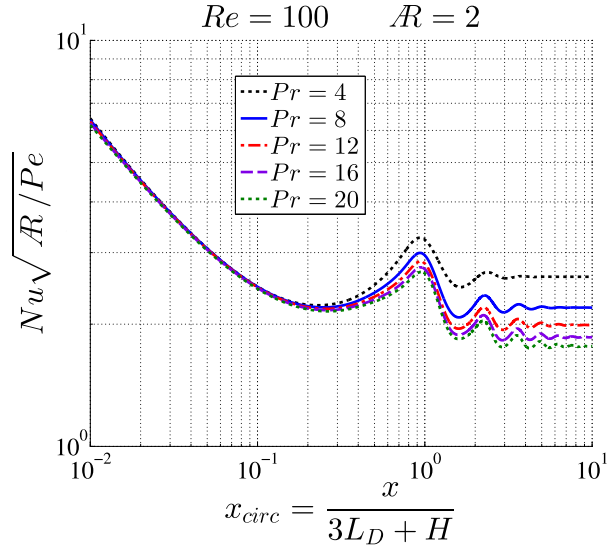

Fig. 15. Scaled Nu with respect to x_{circ} in a parallel plate channel for constant wall temperature.

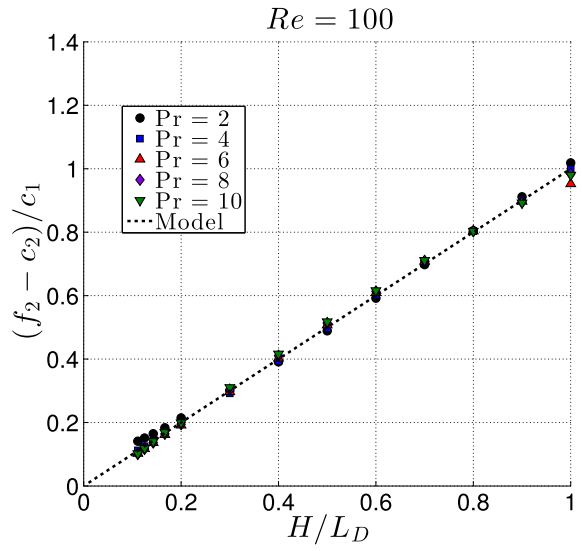

Fig. 16. Scaling constant f_2 with respect to inverse aspect ratio and Pr. Points denote numerical results and line denotes model.

some deviation is observed at low aspect ratios and for low *Pr* values. The deviation at small aspect ratios is attributed to the transition towards a different class of flow, as discussed in Appendix A. In these low $\mathcal{R}$ droplets, the vortices may not necessarily penetrate to the center of the droplet and thus fluid mixing within the droplet is reduced. The divergence at low *Pr* is due to non-negligible streamwise thermal diffusion effects, where heat diffuses faster than it can be convected. For the range *Pr* shown in Fig. 16, streamwise diffusion effects are minimal, however flows with $Pr < 1$ show significant deviations from Eq. (11). It should be noted that due to the slightly different flow fields created by different *Re* values, the scaling above is only applicable to $Re = 100$. However, regardless of *Re*, the scaling constant f_2 maintains a linear relationship with $1/\mathcal{R}$ so that only c_1 and c_2 change. As $\mathcal{R}$ approaches infinity for a droplet, the first term of f_2 in Eq. (11) approaches zero and becomes negligible so that f_2 equals c_2. When *Pr* is equal to one, Eq. (13) predicts that a droplet will have a Nusselt number 3.2 times larger than the equivalent continuous flow. When *Pr* approaches infinity, Eq. (13) predicts that *Nu* for an infinitely long droplet is 5.6 times greater than *Nu* for a continuous flow. This difference can be attributed to the inclusion of interfaces which induce wall normal convection, even in extremely long droplets.

7.6. Scaling of heat transfer (Nu) at all axial distances

Now that f_1 and f_2 have been defined, they can be used to collapse the various *Nu* curves and create a unified curve. In order to smoothly transition between scaling regions, a weight function was defined as

$$w = \frac{1}{\pi}\tan^{-1}(2\pi a(x_{\text{circ}} - b)) + 0.5, \tag{14}$$

where *a* determines how sharp the transition is and *b* determines the location of the transition. The inverse tangent function is chosen as it isolates the effects of f_1 and f_2 to their respective regions and provides a smooth, rapid transition between the two scalings. Combining Eq. (14) with the scaling constants yields

$$Nu^* = Nu[(1/f_1)(1-w) + (1/f_2)w], \tag{15}$$

which results in Fig. 17. In general, *a* and *b* are chosen so that the collapsed curves are smooth. As a guideline, *b* should be on the order of one as this is the separation between the two modes of heat transfer. *a* should be greater than or equal to one because it minimizes the transition region where the *Nu* curve is scaled by a combination of f_1 and f_2. In comparison to previous figures, Fig. 17 shows a set of *Nu* curves that have been approximately collapsed to a single line. While there are slight deviations between the curves for the first few oscillations, this difference quickly diminishes and is barely observable by the second peak.

Fig. 18 shows the fully scaled plot for a constant heat flux boundary condition where f_1 and f_2 remain the same except that c_1 and c_2 have different coefficients that are defined by

$$\text{Constant wall heat flux}: \quad c_1 = 5.5Pr^{0.31} - 4.7, \tag{16}$$

$$c_2 = 0.82Pr^{-0.22} + 3.8. \tag{17}$$

In this scaled plot, differences between constant wall temperature and constant wall heat flux are apparent in the pronounced oscillations in Nu^* as well as the varying decay rate within the first circulation length. This variation in slope is limited to flows with low *Pr* where diffusion effects become more dominant. By $Pr = 6$, the curves become indistinguishable. Similar behavior is seen for continuous flow subject to constant wall heat flux at low *Pr* [31].

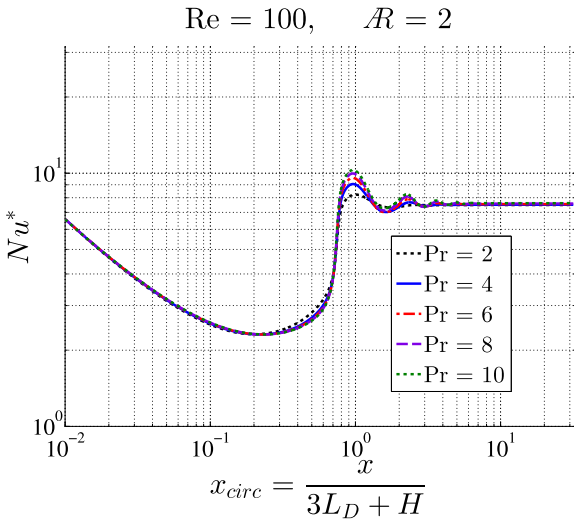

Fig. 17. Nu^* for a droplet between parallel plates subject to constant wall temperature ($a = 5,\ b = 0.75$).

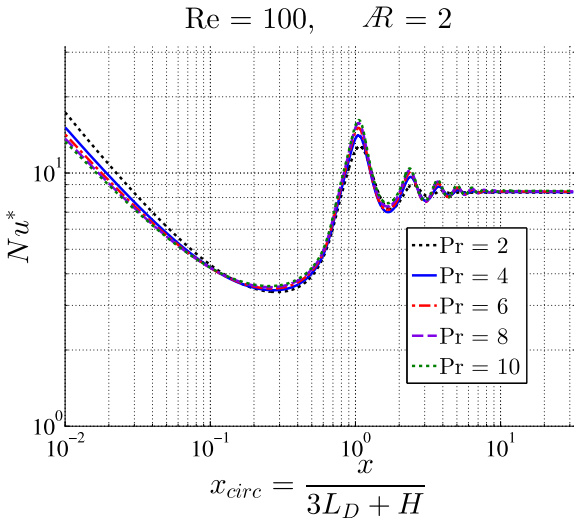

Fig. 18. Nu^* for a droplet between parallel plates subject to constant wall heat flux ($a = 1,\ b = 1$).

7.7. Piecewise equation modeling DHT with constant wall temperature

Motivated by an analysis conducted for the Graetz problem [34,35], a piecewise set of functions are defined for the collapsed DHT *Nu* curves. The function approximating Nu^* in DHT is given by

$$Nu^* = \begin{cases} 0.017\ln(x_{\text{circ}})^4 + 0.154\ln(x_{\text{circ}})^3 + \\ 0.908\ln(x_{\text{circ}})^2 + 1.946\ln(x_{\text{circ}}) + 3.608, & 0 \leqslant x_{\text{circ}} < 0.5, \\ 1.732e^{0.848x_{\text{circ}}} + (5.941\times10^{-8})e^{23.28x_{\text{circ}}}, & 0.5 \leqslant x_{\text{circ}} < 0.75, \\ \{7.14e^{-1.312x_{\text{circ}}}\}\{\sin(5(x_{\text{circ}} - 0.75))\} + 7.54, & x_{\text{circ}} \geqslant 0.75. \end{cases}$$

The approximate equations are shown in Fig. 19 and the equations show good agreement with the numerical data at all axial locations.

7.8. Scaling of heat transfer (Nu) by liquid fraction in DHT

Thus far, the heat transfer analysis has been limited to a single droplet, e.g. fluid A, while ignoring heat transfer to fluid B. This is associated with a liquid fraction of $n = L_A/(L_A + L_B) = 1$ or a droplet train with no measurable gap between droplets. By examining a

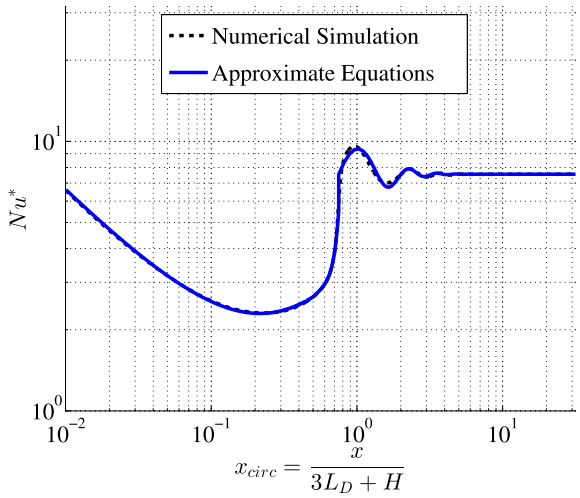

Fig. 19. Comparison of numerical results versus approximate equations for Nu^* in a parallel plate channel with constant wall temperature. $\mathcal{AR} = 2$, $Re = 100$, $Pr = 6$.

fixed axial location along the wall of a microchannel, the results above are extended to flows with $n \neq 1$. If heat transfer at the interface between fluid A and B is ignored, one can analyze heat transfer in one period, $\lambda = L_A + L_B$, by superimposing two droplet trains; one with $k_B = 0$ and one with $k_A = 0$. Based on these assumptions, a two phase flow with the properties given by

$$Re_A = Re_B = 100, \quad \mathcal{AR}_A = 2, \quad \mathcal{AR}_B = 1.33, \quad Pr_A = 6, \quad Pr_B = 1, \quad n = 0.6$$

is subject to constant wall temperature heating. Fig. 20 shows the surface temperature variation versus time at the axial position $x/H = 0.5$. The time along the x-axis was scaled by the period of the flow, which is the time it takes for one droplet of fluid A and B to pass over a given point. As the cool leading edge of the droplet approaches, the axial position experiences a peak in Nu. Shortly afterwards, Nu rapidly decays to a relatively constant value and then experiences a rapid drop as the hot trailing interface passes. These high and low values near the droplet interfaces are localized enough so that Nu is relatively unaffected when averaged over time, and can be approximated using the equations proposed previously. Time averaged Nu values are shown by the dashed lines in Fig. 20.

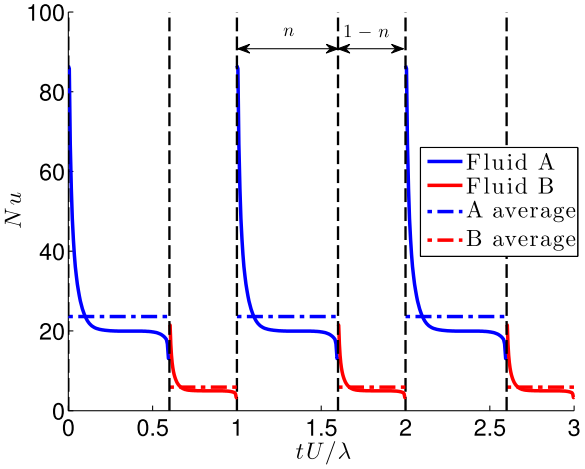

Fig. 20. Nu variation in time at $x/H = 0.5$ within a parallel plate channel subject to constant wall temperature. $Re_A = Re_B = 100$, $Pr_A = 6$, $Pr_B = 1$, $\mathcal{AR}_A = 2$, $\mathcal{AR}_B = 1.33$, $n = 0.6$.

With this approximation, the time varying Nu becomes a square wave where the average Nu observed at any axial location is given by

$$Nu_{avg} = nNu_A + (1 - n)Nu_B. \tag{18}$$

At this point, it has been shown that an initially complex heat transfer problem that is a function of nine distinct dimensional variables (h, H, k, x, ρ, μ, U, c_p, L_D) can be reduced to five non-dimensional parameters (Nu, Re, Pr, x/H, $\mathcal{AR}$). This is further reduced to a single plot of Nu^* vs x_{circ} using the scaling relations derived above. The piecewise equations created provide a simple method of predicting heat transfer at any axial location and show that DHT has a higher Nu than heat transfer in a corresponding continuous flow.

8. Axisymmetric numerical results

In this section, the heat transfer in a digitized flow within an axisymmetric channel is presented. The discussion here is not extensive since the majority of our findings are the same as a parallel plate channel as discussed in detail in previous sections. Instead this section will present key results for completeness and focus on the differences between the two different geometries, such as using D instead of H for all equations and parameters.

Fig. 21 shows typical Nu curves for heat transfer to a digitized flow in an axisymmetric channel for various Prandtl numbers. Similar to the parallel plate channel, flows with higher Pr have larger Nu magnitudes, curves show a constant rate of decay within the first circulation length, and periodic oscillations are apparent after one circulation length. Note that the circulation length in an axisymmetric channel is $2L_D + D$ since the centerline velocity of a droplet is approximately U when observed from a moving reference frame. In contrast to parallel plate heat transfer, the first peak in the Nu plot is sharper and decays rapidly afterwards. This can be attributed to the geometric stretching in the radial direction that gives an axisymmetric channel a better surface area to volume ratio. For an axisymmetric channel, the surface area to volume ratio is $4/D$, where as the ratio for a parallel plate channel is $1/H$. For similarly sized channels where both D and H are equal, an axisymmetric channel has a surface area to volume ratio four times greater than the parallel plate channel. Hence, it is expected that a droplet in an axisymmetric duct will require fewer

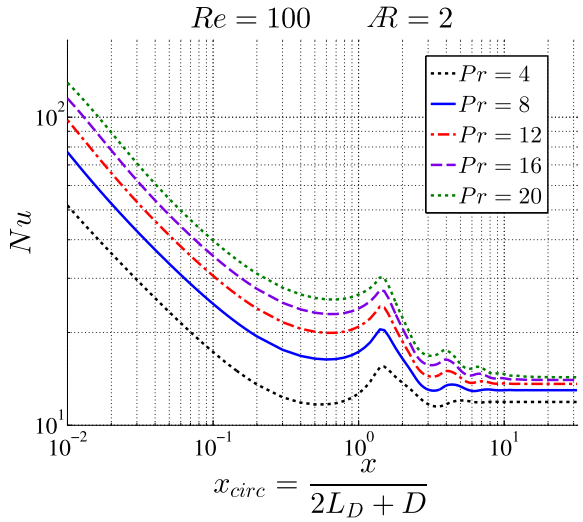

Fig. 21. Nu with respect to x_{circ} for heat transfer in a digitized flow in an axisymmetric channel subject to constant wall temperature.

circulations to reach steady state than an equivalent droplet in a parallel plate channel. Numerical results support this as Fig. 21 shows the axisymmetric *Nu* curve for $Pr = 20$ reaching steady state after four peaks rather than the five peaks observed for the equivalent flow in Fig. 11. While not shown, *Re* and $\mathcal{R}$ have the same effects discussed previously, where an increase in *Re* or a decrease in $\mathcal{R}$ will result in higher *Nu*.

Using the same analysis that was conducted for the parallel plates, it was found that within the first circulation length, the scaling constant f_1 remains as $\sqrt{Pe/\mathcal{R}}$. For axial distances greater than one circulation length, the coefficients for the scaling constant f_2 are given by

$$\text{Constant wall temperature}: \quad c_1 = -9.74Pr^{-0.083} + 10.19, \tag{19}$$

$$c_2 = -8.58Pr^{-0.01} + 10.97 \tag{20}$$

for $Re = 100$. f_1 and f_2 are combined using the Eq. (14) where a is set to 2 and b is set to 1.2. The resulting Nu^* curves are shown in Fig. 22.

The equations that approximate Nu^* for digitized flow subject to constant wall temperature in an axisymmetric channel are given by

$$Nu^* = \begin{cases} -0.003\ln(x_{\text{circ}})^4 + 0.062\ln(x_{\text{circ}})^3 + \\ 0.083\ln(x_{\text{circ}})^2 + 0.065\ln(x_{\text{circ}}) + 0.919, & 0 \leqslant x_{\text{circ}} < 0.5, \\ 0.942e^{-0.059x_{\text{circ}}} + (8.374\times10^{-4})e^{6.308x_{\text{circ}}}, & 0.5 \leqslant x_{\text{circ}} < 1.3, \\ \{4.726e^{-0.919x_{\text{circ}}}\}\{\sin(2(x_{\text{circ}} - 1.1))\} + 3.36, & x_{\text{circ}} \geqslant 1.3. \end{cases}$$

9. Experimental results

9.1. Surface temperature and measurement error

In this section, heat transfer in a digitized flow is characterized by recording the surface temperature of the channel with the set up described in Section 4. Fig. 23 shows the test channel surface temperature from a DHT test along with the predicted bulk fluid temperature, and the surface temperature of a continuous flow with the same *Re* and *Pr*. The surface temperature for DHT shows several oscillations in temperature at small axial distances but quickly settles at a constant growth rate, indicating thermal steady state. In comparison to the continuous flow, the digitized flow reaches steady state at significantly lower axial distances indicating higher heat transfer rates.

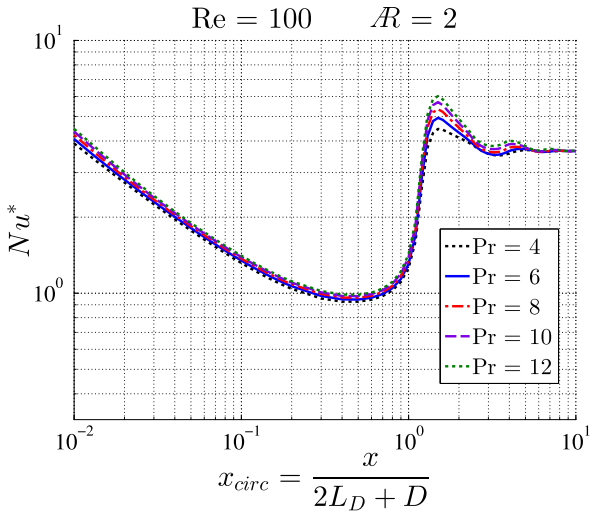

Fig. 22. Nu^* with respect to x_{circ} for constant wall temperature in an axisymmetric channel. $a = 2$, $b = 1.2$.

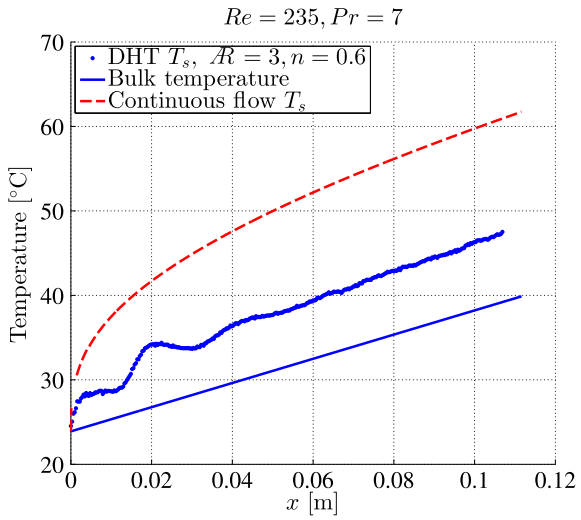

Fig. 23. Instantaneous bulk (solid line) and surface temperature (T_s) for continuous (dashed line) and digitized flows (dotted line) with $Re = 235$.

To ensure that surface temperature measurements were precise, every test used 10 samples to determine the mean surface temperature. The variance of the surface temperature profiles for a typical test are shown in Fig. 24. The largest variance recorded was 0.12 °C where other tests showed similar or smaller variances in temperature. Using a t-distribution with a sample size of 10 yields a 95% confidence interval of $T_s \pm 0.25$ °C. The nondimensional heat transfer rate, *Nu*, was calculated using

$$Nu = \frac{q''D}{k(T_s - T_b)}. \tag{21}$$

Measurement errors propagated from T_s results in a confidence interval of $Nu \pm Nu\frac{0.25}{T_s - T_b}$. For any difference between surface and bulk temperature greater than 5 °C, the error is less than 5% of the true *Nu* value. Due to this small potential error, error bars are not included in the following figures.

9.2. Experimentally observed effects of $\mathcal{R}$ and Re on Nu for DHT

In Section 5, it was identified that $\mathcal{R}$, *Pe*, and x/D would influence heat transfer. This was later confirmed by numerical results and the matching experimental results are shown in Figs. 25 and 26. In Fig. 25, *Nu* is scaled by the liquid fraction for three digitized flows with similar *Pe* values, but varying aspect ratios are shown. As predicted by the simulation and model reported by Baird and Mohseni [13], smaller aspect ratios correspond to higher overall *Nu* magnitudes and exhibit larger number of oscillations before reaching steady state. Furthermore, the first peak in *Nu* falls at approximately one circulation length regardless of aspect ratio. Interestingly, subsequent peaks do not fall at multiples of the circulation length but become more spread out depending on the aspect ratio. Flows characterized by smaller $\mathcal{R}$ have peaks that are further apart than flows with large $\mathcal{R}$. This is due the hydrophilic nature of the channel that creates contact angles less than 90°. The sharp corners of the droplet reduce the circulation within the droplet but since they are of fixed size, they become less significant as $\mathcal{R}$ increases. Aside from different spacing between peaks, there is not a significant difference in shape between the various flows.

Fig. 26 shows several digitized flows with *Re* ranging from 137 to 372. For a direct comparison of *Re*, flows denoted by "◦" and "◇" can be used as they both have an aspect ratio equal to 2.46. Due to shorter circulation times, it is expected that higher *Re* values

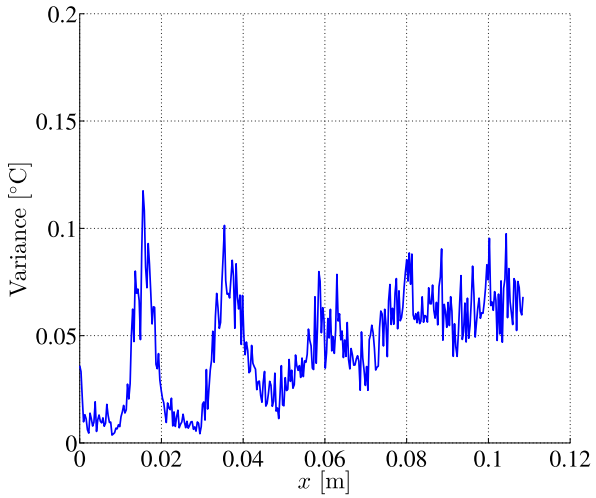

Fig. 24. Variance of the ten surface temperature profiles used to compute *Nu*. $Re = 235,\ \mathcal{AR} = 3,\ n = 0.6,\ Pr = 7$.

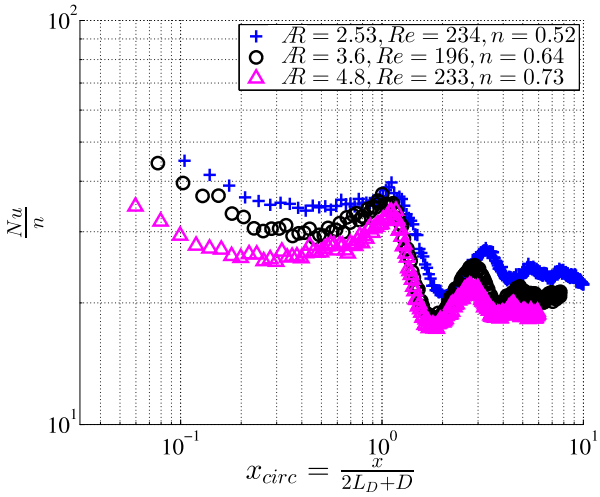

Fig. 25. *Nu* scaled by liquid fraction for heat transfer to digitized flows with $Pr = 7$, similar *Re*, and varying $\mathcal{AR}$.

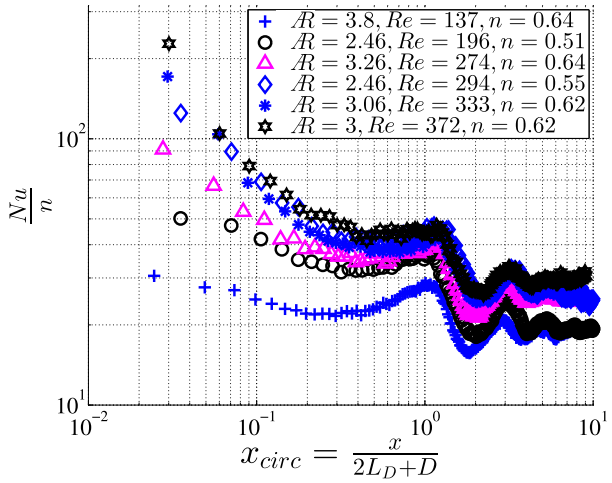

Fig. 26. *Nu* scaled by liquid fraction for heat transfer to digitized flows with $Pr = 7$ and varying *Re*.

correlate to larger *Nu* magnitudes and this is confirmed by the experimental results. Another interesting aspect of this figure is the slope of the *Nu* curve as x_{circ} approaches zero. As *Re* increases, *Pe* increases as well and the *Nu* curves show a steeper initial rate of decay. Since conductive heat transfer is constant due to the constant heat flux boundary condition, this suggests that the convective heat transfer in digitized flows decreases at a faster rate in flows with higher *Pe*. This behavior has been observed in the Graetz problem as well as the numerical simulations conducted previously. However, the Graetz problem converges to a constant slope for $Pe > 50$ [32]. For DHT, the *Nu* curves do not converge until *Pe* is approximately 2500. This difference is attributed to the wall normal velocity that is primarily responsible for increases in convective heat transfer in digitized flows. Changes in *Pe* will have larger effects on convection in digitized flows and thus larger differences in slope at low x_{circ} are expected.

9.3. Scaling of experimental heat transfer (Nu)

After verifying the relationship between $\mathcal{AR}$ and *Re* on *Nu*, the next step is to look at the effectiveness of the derived scaling on the experimental results. Fig. 27 shows the Nu/n scaled by $f_1 = \sqrt{Pe/\mathcal{AR}}$. Similar to the numerical results, scaling by f_1 shows an excellent collapse of data near one circulation length but breaks down at larger axial distances. Additionally, the differences in slope due to *Pe* noted previously are more apparent in this scaled form.

Fig. 28 shows the experimentally measured scaling constant f_2 for $Re = 200$. For the range of aspect ratios tested, the steady state *Nu* shows good agreement with a scaling constant given by the best fit line:

$$f_{2,\exp} = \frac{5.14}{\mathcal{AR}} + 3.27. \tag{22}$$

Based on Eq. (22), the worst case scenario (infinitely long droplet) would still achieve a steady state Nusselt number more than three times greater than a continuous flow. For $\mathcal{AR} = 1$, a steady state Nusselt number over eight times larger than the equivalent continuous flow is predicted.

Using $f_1 = \sqrt{Pe/\mathcal{AR}}$ and $f_{2,\exp}$ given by Eq. (22), scaling is applied to all axial distances using Eq. (15) which results in Fig. 29. Within the first circulation length, the various flows match well in terms of magnitude and rate of decay, indicating the effectiveness of f_1. At

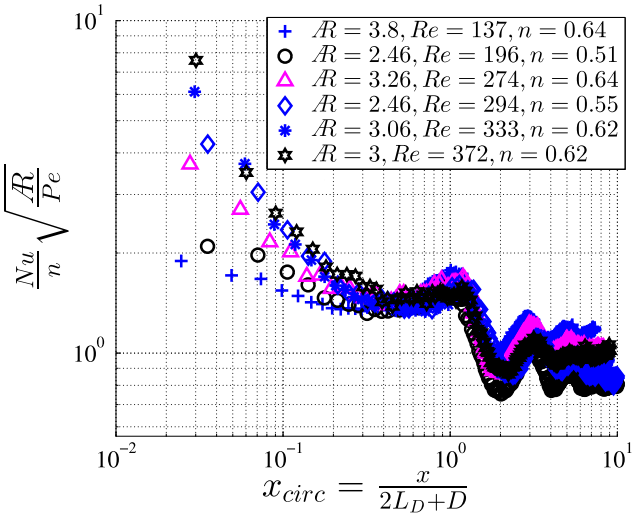

Fig. 27. *Nu* scaled by liquid fraction and f_1 for heat transfer to various digitized flows with $Pr = 7$.

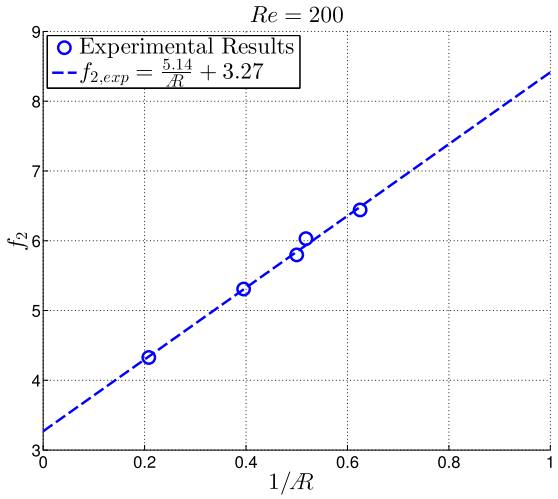

Fig. 28. Experimental steady state *Nu* for digitized flows with $Re = 200$ and $Pr = 7$ compared to $f_{2,exp}$.

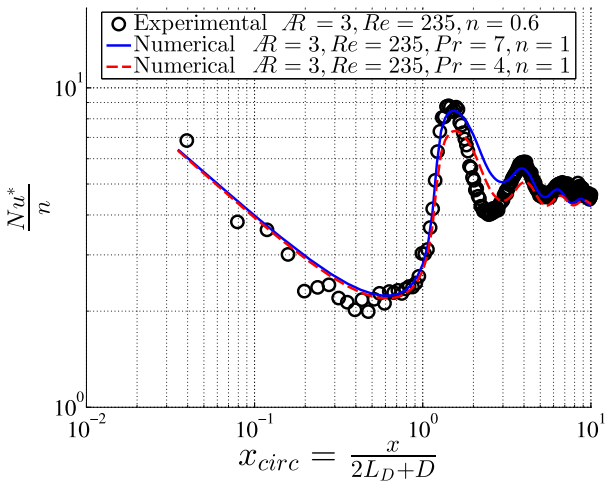

Fig. 30. Numerical versus experimental Nu^* for a digitized flow including bubble expansion effects.

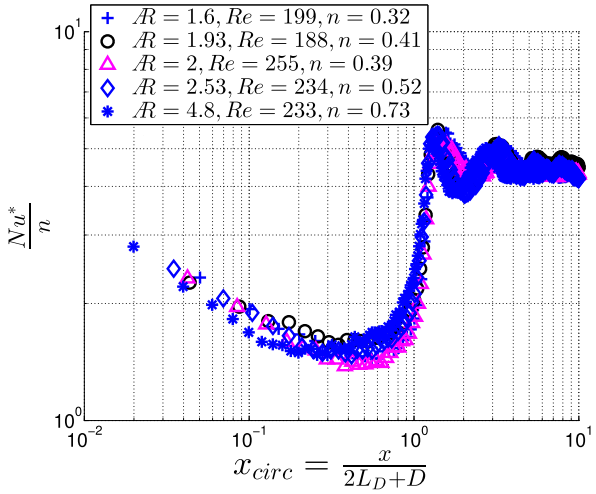

Fig. 29. Nu^* for various digitized flows with $Pr = 7$. $a = 2$, $b = 1.2$ for weighting function.

large axial distances where Nu^*/n has reached steady state, the various curves approach an expected value of 4.36, as dictated by Eq. (10). Overall the scaling shows a collapse of data at both small and large axial distances creating a unified model for DHT.

9.4. Experimental versus numerical heat transfer

In this final section, experimental measurements are directly compared to the numerical simulations for DHT in an axisymmetric microchannel subject to constant heat flux in Fig. 30. In initial comparisons, experimental data showed that flows with large liquid fractions, *n*, exhibited oscillations in *Nu* that occurred at smaller axial distances than predicted, as seen in Fig. 25. This shift in the *Nu* peaks indicated an experimental circulation length that was shorter than expected and can be attributed to air bubble expansion. The low specific heat of air led to high temperatures and ultimately resulted in the increase of bubble volume. In flows where *n* was low, there was a large pressure drop across the channel [36], and thus expansion was limited. In flows with large *n*, the pressure was lower and thus air bubbles expanded and reduced the thermal circulation length of the liquid droplet. The flows reported in this investigation were not significantly affected by bubble expansion, however future studies at high liquid fractions may need to take this effect into consideration.

In Fig. 30, the axial distance, *x* has been scaled using a droplet length that has been decreased by 1.5 mm to account for bubble expansion. With this correction, results show matching *Nu* peaks and the same decay in *Nu* within the first circulation length. Due to the shorter circulation length, hot fluid at the edges of the vortices does not have as much time to mix with the cooler vortex cores. Therefore, when the hot fluid recirculates back to the wall, it is hotter than predicted and results in a steep drop in *Nu* that is most prominent immediately after the first peak. In Fig. 30, the numerical simulation for $Pr = 4$ is also shown to account for possible variations in *Pr* based on rising fluid temperature as the droplet travels along the channel. Aside from the first valley in *Nu*, experimental results behave as expected. While the difference at the first valley appears to be large, it is exaggerated due to the logarithmic scale and in reality the experiment measures a minimum of 4.0 and simulation predicts a minimum of 4.4. Overall, the simulation and experiment show reasonable agreement which indicates that the simplified numerical model is capable of predicting heat transfer to a digitized flow accurately.

10. Conclusion

Throughout this paper, an investigation of the heat transfer characteristics in a digitized flow within a microchannel was conducted. An initial scale analysis found that the heat transfer can be defined by the nondimensional parameter *Nu* which is a function of *Re*, *Pr*, x/H, and L_D/H (x/D and L_D/D in a circular channel). Following the scale analysis, numerical simulations were conducted for heat transfer in a digitized flow within a parallel plate and axisymmetric channel subject to either constant wall temperature or constant heat flux. Results showed that the heat transfer initially experienced exponential decay, transitioned to periodic oscillations, and then progressed to steady state. Through various simulations, it was found that *Nu* has a positive correlation with *Re* and *Pr*. Furthermore, it was determined that the transition between the exponential decay and the period of the oscillations were correlated to a circulation time, that is $(3L_D + H)/U$ in a parallel plate channel and $(2L_D + H)/U$ in an axisymmetric channel. Using the derivation of the Graetz number as a model, axial distance was scaled by the circulation length in order to create the scaled axial distance, x_{circ}, that aligns the various oscillations found in a *Nu*

curve for digitized flows. To further collapse the various *Nu* curves associated with DHT, *Nu* scaling was derived for the two different heat transfer regimes observed. In the first region that was characterized by the exponential decay of *Nu* and x_{circ} less than one, a scaling constant f_1 was found that was approximately equal to $\sqrt{Pe/\mathcal{AR}}$. In the second region, a scaling constant f_2, was found to have a linear relationship with the inverse of the droplet aspect ratio where the coefficients are dependent on *Pr*. Using a weighting function *w*, a scaled Nusselt number, Nu^*, was defined as $Nu[(1/f_1)(1-w)+(1/f_2)w]$ such that a plot of Nu^* vs x_{circ} collapses the various Nusselt curves associated with DHT into a single, unified curve. This analysis allows for approximate analytical equations to be defined so that users are able to predict the heat transfer at any axial location for any $\mathcal{AR}$, flow rate, or fluid.

In addition to numerical simulations, this investigation included experimental tests of heat transfer to a digitized flow in an axisymmetric microchannel subject to constant heat flux. An inverse correlation between *Nu* and $\mathcal{AR}$ was confirmed and a direct relationship between *Nu* and *Re* was observed. Application of the scaling constant f_1 showed convergence of the various *Nu* curves within the first circulation length and also highlighted differences in the initial rate of decay of *Nu* for various *Pe* values. Analysis of steady state *Nu* showed a linear relationship between *Nu* and $1/\mathcal{AR}$ as predicted by numerical simulations. Based on the method used to scale the numerical Nusselt curves, a scaling constant $f_{2,exp}$ for axial distances greater than one circulation length was derived. Using a weighting function to apply f_1 and $f_{2,exp}$ over all axial distances, the experimental *Nu* curves for DHT were collapsed. Numerical simulations were compared with experimental tests where they showed agreement in shape and magnitude. Small deviations in *Nu* peak locations were observed, however it was determined to be the result of expanding air bubbles and was limited to flows with large liquid fractions. Accounting for bubble expansion shifts the experimental *Nu* peaks and good agreement between experiment and simulation is achieved. Throughout this investigation, DHT has been examined using scale analysis, numerical simulations, and experimental measurement in order to define a unified model. In the future, this will hopefully simplify additional work in this field and provide simple approximations for DHT based thermal management solutions.

Conflict of interest

None declared.

Acknowledgment

Financial support for this work was received from the Office of Naval Research and the Thermal Transport Processes program as a part of the National Science Foundation.

Appendix A. Droplet hydrodynamics

While droplet hydrodynamics are not the main focus of this paper, it is still important to look at the effects of *Re* and $\mathcal{AR}$ on the internal flow of a translating droplet, as it can significantly affect heat transfer. Figs. 7 and 8 show a droplet flow field for moderate $\mathcal{AR}$ and *Re*. However, this type of flow is not always apparent and deviations are seen at low aspect ratios and high Reynolds numbers. Fig. A.31(a) and (b) present *u* velocity profiles at the center of the droplet where each profile is shifted slightly to emphasize the differences in shape. When $\mathcal{AR}/Re$ is extremely small, the velocity profile develops a non-parabolic shape which is characterized by higher velocities at the center of the channel and near the walls. If $\mathcal{AR}/Re$ is sufficiently small, then inflection

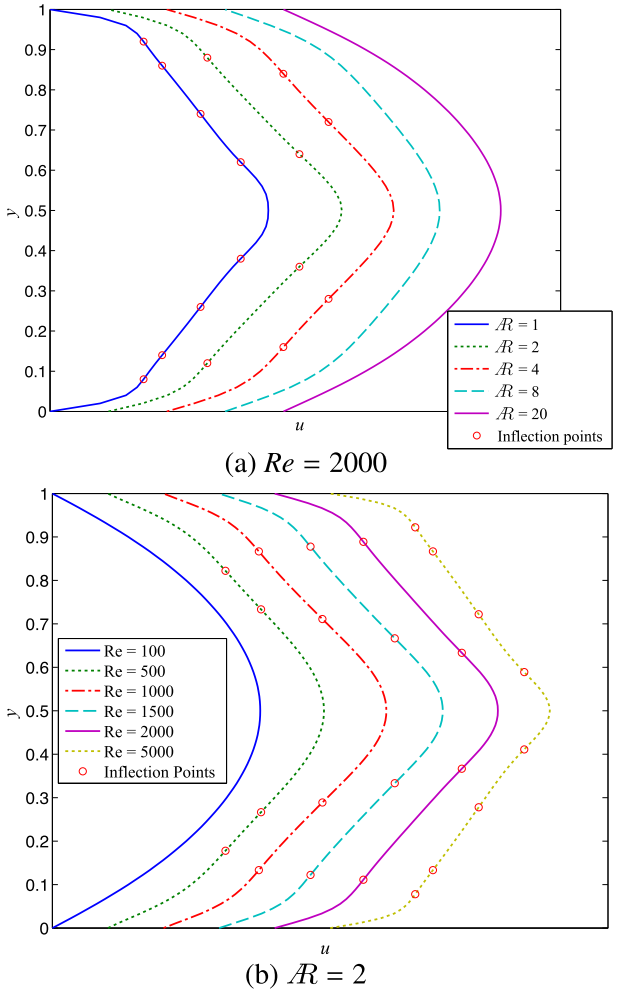

Fig. A.31. Steady state *u* velocity profiles at $x' = 0.5L_D$ for a droplet in a parallel plate channel.

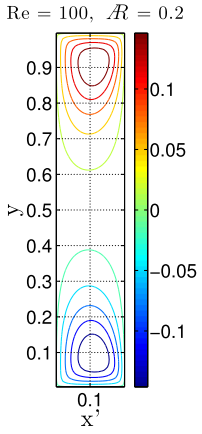

Fig. A.32. Steady state streamlines for a low aspect ratio droplet in a parallel plate channel from a moving reference frame.

points (denoted by dots) are observed. This indicates that the flow is susceptible to turbulence. Based on this observation, heat transfer was only considered for flows with moderate values of $\mathcal{AR}/Re$ that did not exhibit inflection points since turbulent heat transfer is outside the scope of this paper.

Another area of interest was droplets with aspect ratios less than one. This was motivated by the higher heat transfer rates that

were observed for low $\mathscr{R}$ in [13,19]. After simulating a variety of droplet aspect ratios less than one, it was observed that the flows settled at a steady state that no longer resembled the flow seen in Fig. 7. Instead of having two counter rotating vortices that extend to the center of the channel, the droplet flow field is characterized by two vortices near the wall that are separated by a region with no wall normal velocity, as seen in Fig. A.32. While this type of flow was observed in 2D simulations, it is unlikely that droplets with such a low aspect ratio would remain stable in real world flows. Instead, the flow would likely settle into an annular or bubbly flow. Based on the observed flow fields, droplets with aspect ratios less than one are excluded from this study as the heat transfer characteristics are significantly different.

References

[1] I. Mudawar, Assessment of high-heat-flux thermal management schemes, IEEE Trans. Compon. Packag. Technol. 24 (2) (2001) 122–141.
[2] P. Wang, A. Bar-Cohen, On-chip hot spot cooling using silicon thermoelectric microcoolers, J. Appl. Phys. 102 (3) (2007) 034503.
[3] M. Ebadian, C.X. Lin, A review of high-heat-flux heat removal technologies, J. Heat Transfer 133 (11) (2011) 359–366.
[4] D. Kercher, J.-B. Lee, O. Brand, M. Allen, A. Glezer, Microjet cooling devices for thermal management of electronics, Proc. IEEE Trans. Compon. Packag. Technol. 26 (2003) 359–366.
[5] A. Shakouri, J. Bowers, Heterostructure integrated thermionic coolers, Appl Phys Lett 71 (9) (1997) 1234–1236.
[6] A. Shakouri, C. Labounty, P. Abraham, J. Piprek, J. Bowers, Enhanced thermionic emission cooling in high barrier superlattice heterostructures, in: Material Research Society Symposium Proceedings, vol. 545, 1998, pp. 449–458.
[7] J. Fluerial, A. Borshcevsky, M. Ryan, W. Phillips, E. Kolawa, T. Kacisch, R. Ewell, Thermoelectric microcoolers for thermal management applications, in: Proceedings of the IEEE Conference on Thermoelectrics, 1997, pp. 641–645.
[8] S.V. Garimella, C.B. Sobhan, Transport in microchannels-a critical review, Annu. Rev. Heat Transfer 13 (2003).
[9] I. Silverman, A. Yarin, S. Reznik, A. Arenshtam, D. Kijet, A. Nagler, High heat-flux accelerator targets: cooling with liquid metal jet impingement, Int. J. Heat Mass Transfer 49 (17) (2006) 2782–2792.
[10] H. Hirshfeld, I. Silverman, A. Arenshtam, D. Kijel, A. Nagler, High heat flux cooling of accelerator targets with micro-channels, Nucl. Instrum. Methods Phys. Res. Sect. A: Accelerators Spectrometers Detectors Associated Equipment 562 (2) (2006) 903–905.
[11] V. Pamula, K. Chakrabarty, Cooling of integrated circuits using droplet-based microfluidics, in: Proc. ACM Great Lakes Symposium on VLSI, 2003, pp. 84–87.
[12] K. Mohseni, Effective cooling of integrated circuits using liquid alloy electrowetting, in: Proceedings of the Semiconductor Thermal Measurement, Modeling, and Management Symposium (SEMI-Therm), IEEE, San Jose, CA, USA, 2005.
[13] E. Baird, K. Mohseni, Digitized heat transfer: a new paradigm for thermal management of compact micro-systems, IEEE Trans. Compon. Packag. Technol. 31 (1) (2008) 143–151.
[14] T. Jones, On the relationship of dielectrophoresis and electrowetting, Langmuir 18 (2002) 4437–4443.
[15] A. Wixforth, Acoustically driven planar microfluidics, Superlattices Microstruct. 33 (5) (2003) 389–396.
[16] T. Sammarco, M. Burns, Thermocapillary pumping of discrete drops in microfabricated analysis devices, AIChE J. 45 (2) (1999) 350–366.
[17] F. Mugele, J. Baret, Electrowetting: from basics to applications, J. Phys.: Condens. Matter 17 (28) (2005) R705–R774.
[18] W. Nelson, C.-J. Kim, Droplet actuation by electrowetting-on-dielectric (EWOD): a review, J. Adhes. Sci. Technol. 26 (12–17) (2012) 1747–1771.
[19] P. Walsh, E. Walsh, Y. Muzychka, Heat transfer model for gas–liquid slug flows under constant flux, Int. J. Heat Mass Transfer 53 (15) (2010) 3193–3201.
[20] A. Mehdizadeh, S. Sherif, W. Lear, Numerical simulation of thermofluid characteristics of two-phase slug flow in microchannels, Int. J. Heat Mass Transfer 54 (15) (2011) 3457–3465.
[21] N. Kumari, S. Garimella, Characterization of the heat transfer accompanying electrowetting or gravity-induced droplet motion, Int. J. Heat Mass Transfer 54 (17) (2011) 4037–4050.
[22] A. Betz, D. Attinger, Can segmented flow enhance heat transfer in microchannel heat sinks?, Int J. Heat Mass Transfer 53 (19) (2010) 3683–3691.
[23] A. Asthana, I. Zinovik, C. Weinmueller, D. Poulikakos, Significant Nusselt number increase in microchannels with a segmented flow of two immiscible liquids: an experimental study, Int. J. Heat Mass Transfer 54 (7) (2011) 1456–1464.
[24] D. Lakehal, G. Larrignon, C. Narayanan, Computational heat transfer and two-phase flow topology in miniature tubes, Microfluidics Nanofluidics 4 (4) (2008) 261–271.
[25] J. Howard, P. Walsh, E. Walsh, Prandtl and capillary effects on heat transfer performance within laminar liquid–gas slug flows, Int. J. Heat Mass Transfer 54 (21) (2011) 4752–4761.
[26] P. Zhang, K. Mohseni, Numerical investigations of digitized heat transfer, in: ICNMM 2012-73297, ASME 2012 International Conference on Nanochannels, Microchannels, and Minichannels, Rio Grande, Puerto Rico (July 8–12 2012).
[27] P. Zhang, K. Mohseni, Numerical and experimental investigation of heat transfer within the first circulation length of a digitized flow, in: Proceedings of the Semiconductor Thermal Measurement, Modeling, and Management Symposium (SEMI-Therm), IEEE, San Jose, CA, USA, 2013.
[28] M. Kreutzer, F. Kapteijn, J. Moulijn, J. Heiszwolf, Multiphase monolith reactors: chemical reaction engineering of segmented flow in microchannels, Chem. Eng. Sci. 60 (22) (2005) 5895–5916.
[29] H. Song, D. Chen, R. Ismagilov, Reactions in droplets in microfluidic channels, Angew. Chem. Int. Ed. 45 (44) (2006) 7336–7356.
[30] F. Harlow, J. Welch, Numerical calculation of time-dependent viscous incompressible flow of fluid with free surface, Phys. Fluids 8 (1965) 2182.
[31] A. Bejan, Convection Heat Transfer, second ed., Wiley-Interscience, United States, 1994.
[32] R. Shah, A. London, Laminar flow forced convection in ducts: a source book for compact heat exchanger analytical data, Advances in heat transfer: Supplement, Academic Press, 1978. <http://books.google.com/books?id=HkmWuooiMWAC>.
[33] E. Buckingham, On physically similar systems; illustrations of the use of dimensional equations, Phys. Rev. 4 (1914) 345–376, http://dx.doi.org/10.1103/PhysRev.4.345. <http://link.aps.org/doi/10.1103/PhysRev.4.345>.
[34] U. Grigull, H. Tratz, Thermischer einlauf in ausgebildeter laminarer rohrströmung, Int. J. Heat Mass Transfer 8 (5) (1965) 669–678.
[35] R. Shah, Thermal entry length solutions for the circular tube and parallel plates, in: Proceedings of the Third National Heat Mass Transfer Conference, vol. 1, 1975.
[36] M. Kreutzer, F. Kapteijn, J. Moulijn, C. Kleijn, J. Heiszwolf, Inertial and interfacial effects on pressure drop of Taylor flow in capillaries, AIChE J. 51 (9) (2005) 2428–2440.